Erosional control of the kinematics and geometry of fold-and-thrust belts imaged in a physical and numerical sandbox

L. Cruz,[1] J. Malinski,[1] A. Wilson,[1] W. A. Take,[2] and G. Hilley[1]

[1]   We investigate the effect of systematically varying erosion intensity (K) on the geometry and kinematics of fold-and-thrust belts modeled using equivalent conditions in physical and numerical experiments. Similar material properties and boundary conditions were used to compare numerical experiments to those modeled in the sandbox using an erosion rule that removes mass from the scaled sand wedges according to rates expected from bedrock fluvial incision. The geometry of both modeling approaches is quantitatively compared with that expected from analytical theory. The fold-and-thrust belt growth rate is inversely proportional to K and is well predicted by theory, except for the high erosion case, in which both the numerical and the experimental sandbox grows supercritically. A direct relationship exists between the erosion intensity and the number of fore-shear bands and shear strain magnitude. The number of fore-shear bands decreases, and their strain increases with erosion intensity. The results indicate that realistic and mechanistic erosion rules can be applied to physical experiments to model mass removal, and this approach opens up the possibility of calibrating strain history to erosion intensities for predictions in natural settings. Quantitative comparisons between the physical and numerical sandbox experiments indicate that deformation style and geometry of the thrust-and-fold belts are similar when identical rheologies and boundary conditions are used. This benchmarking suggests that numerical experiments realistically model conditions observed in the simple, cohesionless rheologies commonly employed in sandbox experiments. This suggests that numerical simulation may reliably model experimental deformation in geological situations that are difficult to represent in scaled experiments because of the different scales and rheologies of natural orogenic wedges.

1. Introduction

[2]   Geologic evidence and modeling studies indicate that erosion exerts a primary control on the evolution of orogenic wedges [e.g., *Beaumont et al.*, 1992; *Willett*, 1999; *Willett and Brandon*, 2002; *Davis et al.*, 1983; *Dahlen et al.*, 1984; *Dahlen*, 1984; *Mulugeta and Koyi*, 1987; *Dahlen and Suppe*, 1988; *Dahlen and Barr*, 1989; *Barr and Dahlen*, 1989; *Hilley et al.*, 2004; *Hilley and Strecker*, 2004; *Grujic et al.*, 2006]. This occurs because erosion redistributes mass across Earth's surface, which modifies the near-surface lithostatic stresses. Changes in the stress state may alter stable structural geometries (i.e., critical wedge

geometry [*Davis et al.*, 1983; *Dahlen et al.*, 1984; *Dahlen*, 1984]), which affects the lateral growth and internal deformation of orogenic wedges.

[3]   Sandbox models that have been scaled to natural orogens have also been used to study the interactions between erosion and deformation in sand wedges, although simplistic rules are often used to simulate erosion [e.g., *Cobbold et al.*, 1993; *Persson and Sokoutis*, 2002; *McClay and Whitehouse*, 2004; *Konstantinovskaia and Malavieille*, 2005; *Hoth et al.*, 2006; *Cruz et al.*, 2008; *Hoth et al.*, 2008]. However, more mechanistic and realistic erosion rules have recently been developed to model mass removal from orogens [*Hilley et al.*, 2004; *Whipple and Meade*, 2004]. The application of these types of erosion rules in experimental models has been prevented in part by physical limitations associated with human intervention and accuracy. More importantly, no study to our knowledge has used these types of rules to systematically explore the effect of changing erosion intensity on the geometry and kinematics of experimental fold-

---

[1]Department of Geological and Environmental Sciences, Stanford University, Stanford, California, USA.
[2]Department of Civil Engineering, Queen's University, Kingston, Ontario, Canada.
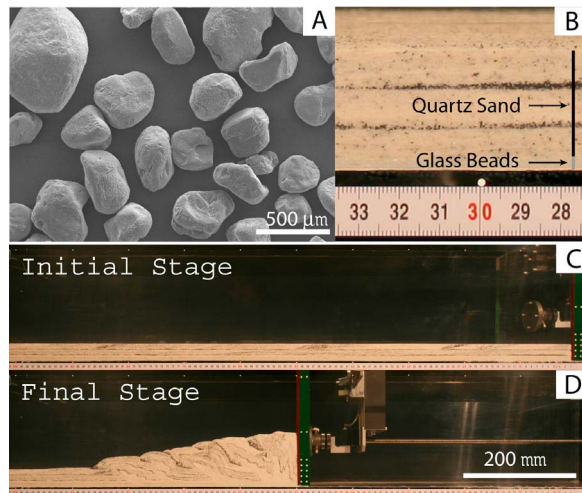
Figure 1. (a) SEM image of the sand mix used to represent upper crustal material. Grain size distributions analysis of the sand mix indicates a peak in the range of 224 to 355 μm, and grain shapes range from angular to well rounded [*Klinkmueller et al.*, 2008]. (b) Photograph of a portion of the initial stage prior to deformation showing the configuration of the glass beads and sand mix layers. (c and d) Initial, before deformation, and final stages, after total deformation, of the physical experiments showing the total extent of displacement imposed during the experiment.

and-thrust belts modeled in the sandbox. Furthermore, the geometric evolution of such models has not been quantitatively compared with that expected from theory [e.g., *Hilley et al.*, 2004] or numerical simulations.

[4] Here, we present results from theoretical, experimental, and numerical frontally accreting orogenic wedges whose surfaces are eroded synkinematically according to an orogen-scale rule, in which mass is primarily exported from the orogen by bedrock fluvial incision [*Hilley et al.*, 2004]. In this study, deformation within the sand wedge is driven by constant displacement rate boundary conditions applied to a moving backstop. In each set of experiments, we systematically varied the bedrock incision coefficient, K, which subsumes the effects of the intensity of erosional properties as well as the properties of the substrate (hereafter, we refer to this as erosional intensity), to compare the geometric evolution of the experimental and numerical simulations with that predicted theoretically [*Hilley et al.*, 2004]. Furthermore, we applied recent advances in non-invasive particle-monitoring techniques (particle image velocimetry, PIV [*Raffel et al.*, 1998]) to quantify the response of the physical sandbox experiments' two-dimensional kinematics to changing erosional efficiency acting over the surface of the simulated orogen for comparison with the kinematics produced in the numerical simulations.

2. Experimental Models of Fold-and-Thrust Belts

2.1. Materials, Design, and Scaling

[5] Deformable materials consisted of a 2-mm layer of glass beads placed at the base of a Teflon-coated box. This

layer served as a scaled detachment horizon or weak layer at the base of the wedge [*Chapple*, 1978]. Next, a 28-mm layer of quartz sand, whose failure envelope is independent of strain rate [e.g., *Davis et al.*, 1983; *Sonder and England*, 1986], was placed on top of the detachment horizon (Figure 1). Approximately 10% of the sand was colored black to increase visual contrast and enhance PIV results. Filling was consistent with standards employed in recent experiments (S. Buiter and G. Schreurs, Geomod2008 Web site, Analogue-numerical comparisons, Setup and modeling procedure for experiments, 2008, http://www.geodynamics. no/benchmarks/benchmark-annum2008.html). Glass beads and sand mix were sieved homogenously with a filing rate of 250ml/min into the sandbox from a height of ~20 cm using a 40-mm-diameter cylindrical device that has 24 holes at the bottom plate: each hole is 2 mm in diameter. Glass beads and sand particles were ~200 μm and ~300 μm in diameter (Figure 1a), respectively. The grain size distribution analysis of the sand mix shows a peak in the range of 224 to 355 μm, and grain shapes (Figure 1a) range from angular to well rounded [*Klinkmueller et al.*, 2008]. The material properties of the granular materials used in this experiments are summarized in Table 1. The internal friction angle of the sand mix (Φ) is ~33° [*Klinkmueller et al.*, 2008], while the interface friction angle of the glass beads against Plexiglas (Φ_b) is ~25°. The sand internal friction angle was calculated using statistical linear regression of the normal and shear stress data points measured with a ring shear tester over a normal stresses range of ~400 to 2150 Pa. The glass beads-Plexiglas interface friction angle was calculated using critical Coulomb theory [*Dahlen*, 1984] and the measured topographic slope. The densities of the sand mix and the glass beads are 1538 and 1407 kg/m³, respectively.

[6] The total thickness of deformable materials was designed to represent ~15 km of brittle upper crust [*Byerlee*, 1978]. Using this length, the model was scaled to a natural orogenic wedge using scaling rules utilized in previous analog models [e.g., *Hubbert*, 1937; *Ramberg*, 1967; *Cobbold et al.*, 1993; *Koyi*, 1997; *Schellart*, 2000; *Persson and Sokoutis*, 2002; *Lohrmann et al.*, 2003; *Persson et al.*, 2004], in which the vertical stress and cohesion of the model and nature have the same units and are scaled similarly. In our experiments, the model/nature vertical stress

Table 1. Summary of Material Properties and Parameters Used in Physical and Numerical Experiments

Parameter	Physical Experiment[a]	Numerical Experiment
Quartz sand		
Density (kg/m³)	1538	1538
Internal friction angle (Φ)	33°	33°
Cohesion (Pa)	57	57
Glass beads (detachment)		
Density (kg/m³)	1407	1407
Internal friction angle (Φ)	NM	30°
Interface friction angle (Φb)	25°[b]	25°
Cohesion (Pa)	NM	50
Gravitational acceleration (m/s²)	9.81	9.81
Background viscosity (Pa s)		10¹²
Time step (years)	continuous	31,524

[a]NM, not measured
[b]Calculated using critical Coulomb theory and the measured topographic slope [*Dahlen*, 1984].
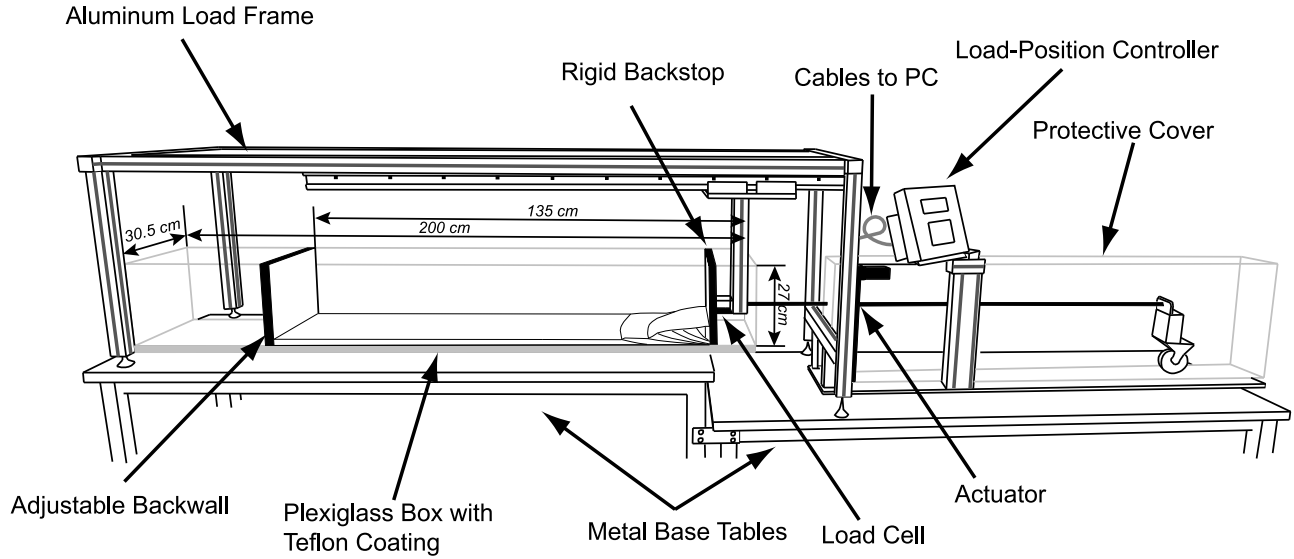
Figure 2. Technical sketch of the experimental apparatus, showing the load frame, servo-controller system and Teflon coated Plexiglas box with internal dimensions. Not shown in this illustration are the three digital cameras, the straight-line-projecting laser, and the dust vacuum.

ratio is ~1.3 × 10^{-6}, and the measured model cohesion is ~57 Pa, which implies a value of ~70 MPa for cohesion of natural rocks, which is representative of the Earth's upper crust [*Goodman*, 1988]. The dimensions of the Plexiglas-Teflon-coated experimental box are 130 cm long, 30.5 cm wide and 28 cm high (Figure 2). The transparent Teflon coating was applied to the Plexiglas walls to reduce sidewall friction. The Plexiglas walls and bottom plate have a thickness of 2.54 cm to ensure rigidity during the experiments. In addition, we designed small metal rollers that were attached to the upper sides of the moving plate to ensure constant width of the box during contraction during the experimental runs.

2.2. Procedure

[7] We deformed four experimental models using a servo-controlled system and a rigid vertical backstop. The backstop was displaced at a constant velocity of 2 mm/min up to ~60 cm or ~46% of the total model length. The experimental apparatus consisted of a high-resolution load-and-position control electromechanical test system that included an aluminum load frame, a load cell, and a PC-controlled servo-controller (Figure 2). In this experimental setting, the scaled orogenic deformation is driven by forces transmitted laterally into the modeled crust [*Peltzer and Tapponnier*, 1988; *England and Houseman*, 1986].

[8] The reference model was deformed but not eroded (Figure 3a), while the others (Figures 3b–3d) were deformed and eroded using different values for the erodibility factor K (Table 2) at specific time steps after 20 cm of model displacement. Using time steps of 2 × 10^6 years, we calculated the mass to be removed according to the surface slope observed during the time step and an orogen-scale erosion rule that regards mass removal rates as limited by fluvial bedrock incision (erosion rule presented by *Hilley et al.* [2004]). In this formulation [*Hilley et al.*, 2004], the wedge develops and deforms at its Coulomb failure limit [*Davis et al.*, 1983], and so the topographic slope (α) to the

basal fault angle (β) may be related to the material properties of the dry sand wedge [*Dahlen*, 1984] according to

$$\beta = \tfrac{1}{2} \arcsin(\sin\varphi_b/\sin\varphi) - \tfrac{1}{2} \sin\varphi_b$$
$$- [\tfrac{1}{2} \arcsin(\sin\alpha/\sin\varphi) - \tfrac{1}{2}\alpha] - \alpha. \quad (1)$$
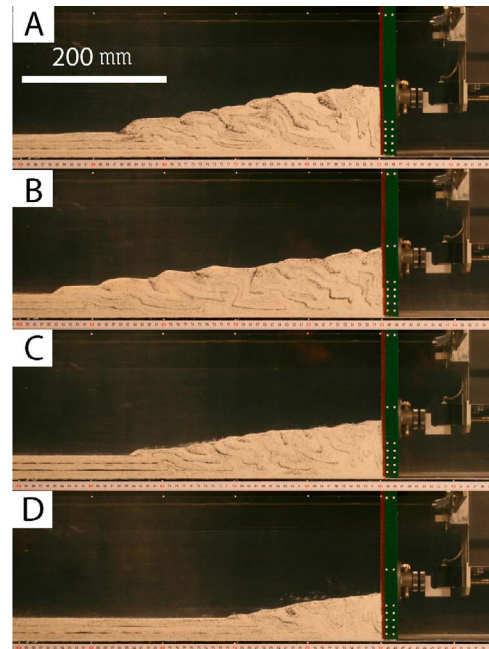

Figure 3. Photographs of the physical experiments after 500 mm of displacement showing wedge width, topography and internal deformation for different erosion intensities. (a) $K = 2.3 \times 10^{-7}$ m$^{0.2}$/yr. (b) $K = 2.3 \times 10^{-6}$ m$^{0.2}$/yr. (c) $K = 1.2 \times 10^{-5}$ m$^{0.2}$/yr. (d) $K = 2.3 \times 10^{-5}$ m$^{0.2}$/yr.

Table 2. Summary of Erosion Rule Model Parameters Used in Physical and Numerical Experiments[a]

Parameter	Physical Experiment	Numerical Experiment
v (mm/yr)	17	17
T (km)	15	15
D (km)	15	15
ka (m$^{0.6}$)	4	4
h	1.4	1.4
m	0.4	0.4
n	1	1
Initial erosion time step ($\times 10^6$ year)	5.7	5.7
Erosion time step $\times 10^6$ year)	2.0	2.0
K (model 1) (m$^{0.2}$/yr)	2.3×10^{-7}	2.3×10^{-7}
K (model 2) (m$^{0.2}$/yr)	2.3×10^{-6}	2.3×10^{-6}
K (model 3) (m$^{0.2}$/yr)	1.2×10^{-5}	1.2×10^{-6}
K (model 4) (m$^{0.2}$/yr)	2.3×10^{-5}	2.3×10^{-5}

[a]See *Hilley et al.* [2004].

[9] Material is eroded according to the bedrock incision rule [*Howard and Kerby*, 1983] such that the volume, or area in our two-dimensional modeling approach that assumes no orogen-parallel transport of material, of eroded material is

$$Fe = \left(Kk_a{}^m S^n W^{hm+1}\right)/(hm + 1), \qquad (2)$$

where Fe is the flux removed, k_a is an area-length coefficient, S is the slope of the sand wedge, W is the width of the orogen, h is an exponent in area-length relationship, m is an area exponent, and n is a slope exponent. A summary of the used erosion-rule model parameters is presented in Table 2. We used values of 4, 1.4, 0.4, and 1 for the parameters ka, h, m, and n, respectively, following *Hilley et al.* [2004]. We fix the depth at which the basal décollement flattens (D), and the wedge is assumed to incorporate mass from the foreland at a volumetric flux equal to [*DeCelles and DeCelles*, 2001]

$$Fa = vT, \qquad (3)$$

where Fa is the flux added, ν is the convergence velocity of the foreland, and T is the thickness of the accreted foreland material. In our case, we assumed a convergence velocity of 17 mm/yr and a material thickness of 15,000 m to match that of *Hilley et al.* [2004].

[10] The wedge changes its cross-sectional area such that it maintains a mechanical balance, and hence the rate of change of the cross-sectional area equals the difference in these volumetric fluxes [*Hilley et al.*, 2004]:

$$da/dt = Fa - Fe, \qquad (4)$$

where da/dt is the rate of change of the cross-sectional area of the wedge. For a given time increment,

$$da/dt = \Delta A/\Delta t = vT - \left(Kk_a{}^m S^n W^{hm+1}\right)/(hm + 1), \qquad (5)$$

where ΔA is the area variation and Δt is the time increment; the area variation for a given time increment is also

$$\Delta A = A_2 - A_1 \qquad (6)$$

and the area of the triangular wedge is

$$A = (1/2)WH \text{ or } A = (1/2)W^2 \tan\alpha, \qquad (7)$$

where H is the height of the wedge. After substituting (7) in (6) and (6) in (5), we can solve for the unknown topographic slope α_2 at the end of each time increment:

$$\alpha_2 = \alpha_1 + \text{atan}\left[\left(2vT/W^2\right) - \left(2Kk_a{}^m S^n W^{hm+1}/hm + 1\right)\Delta t\right], \qquad (8)$$

where α_1 is the initial topographic slope for the given time increment. We use this theory to determine the temporal geometric evolution of the wedge for a prescribed initial geometry (initial surface slope = 0°) and integration time steps of 2×10^6 years, which represents 7 cm of model displacement. In order to transfer the calculated slope to the physical experiment after each time step, a laser line was projected into the sandbox sidewall to guide the removal of sand with a small-nozzle vacuum cleaner. The experiments were never stopped during each erosion event, since the backstop displacement rate was 2 mm/min, which is a rate low enough to remove mass and assume that the erosion event is instantaneous. After the last time step calculation, the low erodibility case didn't yield any mass removal. Therefore, in our results the reference model and the lowest erosion case are the same (Figure 3a).

[11] The models were monitored with a system of three digital cameras, including two on the sides and one on top, which were triggered after every 2 mm of displacement by the servo-controlled system. The cameras were calibrated to enhance image contrast for PIV. This PIV technique has been successfully applied to study geodynamics processes in scaled experiments where detail kinematics is necessary [e.g., *Adam et al.*, 2005; *Hoth et al.*, 2006; *Cruz et al.*, 2008; *Hoth et al.*, 2008].

[12] We computed four forward models using the same parameters and material properties utilized in the physical experiments to compare these results with theoretical expectations. In order to implement this erosion rule in the forward models, we assumed from the theoretical wedge geometry [*Hilley et al.*, 2004] that the initial wedge area is

$$A_1 = (1/2)D^2/\tan\beta_1 \qquad (9)$$

and the wedge area at the end of the first time increment is

$$A_2 = (1/2)D^2/\tan\beta_2[1 - \tan\alpha_2/\tan\beta_2]. \qquad (10)$$

After substituting (9) and (10) in (6) and (6) in (5) and considering that the slope S is $\tan\alpha_1$, we obtain the following expression:

$$\begin{aligned}
1/\tan\beta_2(1 + \tan\alpha_2/\tan\beta_2) \\
= 2\Delta t/D^2\left[vT - \left(Kk_a\tan\alpha_1^n W^{hm+1}\right)/(hm + 1)\right] \\
+ 1/\tan\beta_1(1 + \tan\alpha_1/\tan\beta_1),
\end{aligned} \qquad (11)$$

where β_1 and β_2 are the basal fault angles at the beginning and at the end of the time increment, respectively. We can use (11) to iteratively find the $\alpha_2 - \beta_2$ pair values that satisfy the expression for each time increment.

3. Numerical Models of Fold-and-Thrust Belts

[13] We simulated several frontally accreting fold-and-thrust belts using the Gale numerical package [*Moresi et al.*,
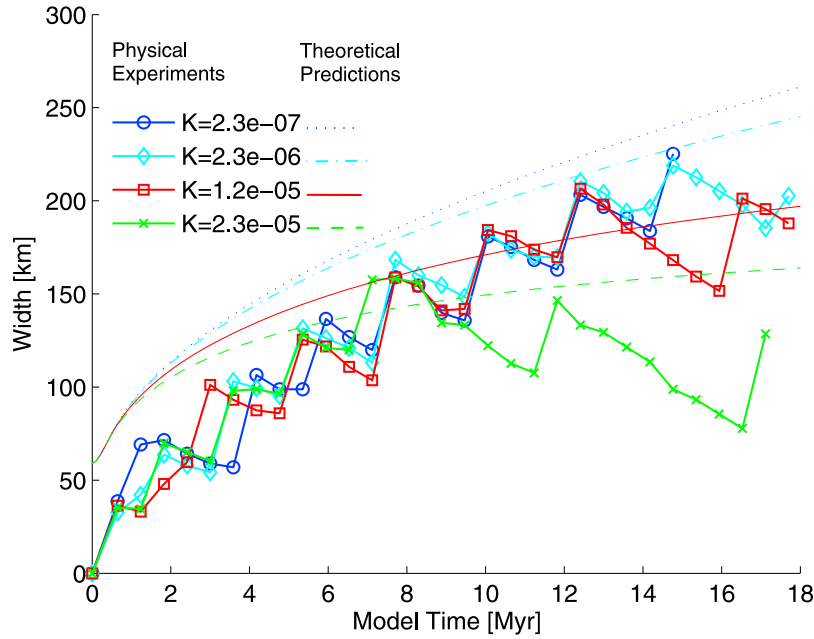
Figure 4. Temporal evolution of the orogenic wedge width observed in the scaled physical experiments (circles, diamonds, squares, and crosses correspond to the measurements of experimental geometries for K values of 2.3×10^{-7} m$^{0.2}$/yr, 2.3×10^{-6} m$^{0.2}$/yr, 1.2×10^{-5} m$^{0.2}$/yr, and 2.3×10^{-5} m$^{0.2}$/yr) and the corresponding theoretical model results (dotted, dash-dotted, solid, and dashed lines correspond to the calculated theoretical simulations with K values of 2.3×10^{-7} m$^{0.2}$/yr, 2.3×10^{-6} m$^{0.2}$/yr, and 1.2×10^{-5} m$^{0.2}$/yr, and 2.3×10^{-5} m$^{0.2}$/yr, respectively).

2003]. Gale is a two- or three-dimensional open-source code that uses particles to track material properties and a finite element mesh, where the Stokes equations are solved, superimposed over the particles to allow for large deformations and complex boundary conditions. We configured the Gale numerical sandbox using the same physical geometries, boundary conditions (including constant-displacement-rate conditions) and material properties (including basal and internal friction, density and cohesion, and layer lengths) that we used in the experimental sandbox. However, we used 2D plane-strain conditions to model the out-of-plane dimension, and as a result, our numerical model does not treat the effect of sidewall friction present in the physical sandbox model. We simulated a low-viscosity (1 Pa · s) air layer on top of the sand layer. We modified the predefined surface process module in Gale, to calculate surface lowering that resulted from the erosion rule used in the experimental sandbox. We used a Drucker-Prager failure criterion that in 2D is equivalent to a Mohr-Coulomb rheology. This failure criterion is defined in the Gale code as

$$\sqrt{J_2} = p * \sin \varphi + C * \cos \varphi, \qquad (12)$$

where J_2 is the second invariant of the deviatoric stress tensor, p is pressure, φ is the internal friction angle, and C is cohesion.

[14] Similar to our experimental sandbox, the first simulation in the numerical sandbox was deformed but not eroded. This was used as a comparison against its experimental counterpart and as a reference for the erosional cases. Four numerical simulations were designed to mimic those simulated physically by using the same values for the erod-

ibility factor K and the same time increments (2×10^6 years) between discrete erosion events that were initiated after 20 cm (5.7×10^6 years) of model displacement.

4. Results

4.1. Temporal Evolution of Orogenic Wedge Geometry

[15] We used values of $K = 2.3 \times 10^{-7}$ m$^{0.2}$/yr, 2.3×10^{-6} m$^{0.2}$/yr, 1.2×10^{-5} m$^{0.2}$/yr, and 2.3×10^{-5} m$^{0.2}$/yr for the erosional efficiency in our experiments, which is roughly consistent with the naturally observed range in this value [*Stock and Montgomery*, 1999] that can realistically be simulated, given the limits of human intervention and the characteristics of our experimental apparatus. The temporal evolution of the scaled experiments' geometries is shown in Figure 4.

[16] Theoretical simulations show a similar orogen widening for the first 2 Myr for all cases (Figure 4), after which widening rate decreases asymptotically to zero. The ultimate width of the wedge varies inversely with K [*Hilley et al.*, 2004] and adjusts over an exponentially growing time that scales with K [*Whipple and Meade*, 2004]. Simulations were runup to 18 Myr of model time, at which point we observed a difference in orogen width of ~100 km between the high and low erosion cases. Physical experiments also showed a rapid wedge widening for the first 2–3 Myr, after which an overall decrease in widening rate was observed [*Koyi*, 1995, *Mulugeta and Koyi*, 1992]. After 18 Myr of model time, the difference in width between the high and low erosion cases was ~100 km (Figure 4). While the consistency between theory and experiments indicate that the sand in the apparatus generally deforms according to Coulomb wedge theory
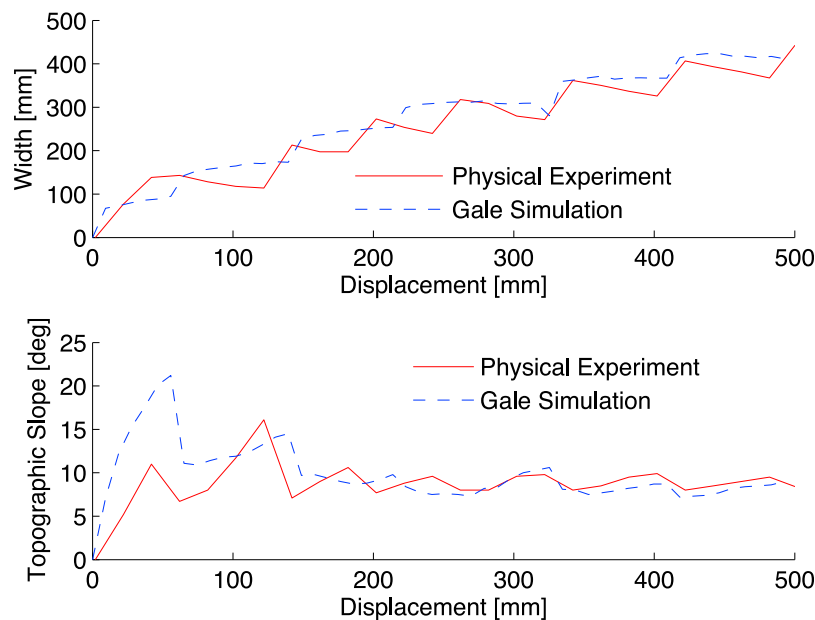
Figure 5. Comparison of simulated orogenic wedge geometry between the no-erosion cases of the experimental and numerical simulations. Wedge width, defined as the distance between the rigid backstop and the fore-most shear band, is plotted versus total displacement of the backstop. The average surface slope, defined as the elevation change over the wedge width, is likewise shown as a function of total displacement. Note the good correlation between the wedge growth and the topographic evolution of both modeling approaches.

[*Dahlen*, 1984], physical experiments showed an episodic step-like growth associated with the development and reactivation of shear bands (thrust) and the consequent adjustment of the topographic slope [*Koyi*, 1995, *Mulugeta and Koyi*, 1992]. The observed pattern of wedge growth is generally well predicted by theory, except for the high erosion case, which predicts a wider wedge geometry after 18 Myr than that observed in the physical experiments, producing a difference of ~35 km. This suggests that this high-erosion case grows in a primarily supercritical manner, which means that the wedge is growing steeper than what it should grow considering its physical properties.

[17] The geometric evolution of the orogenic wedges produced by the Gale numerical simulations showed a good correspondence with their experimental counterparts (Figures 5 and 6). Nonetheless, differences between the physical and numerical simulations are manifest as variations in the timing and the total number of forward shear-band-forming episodes. The numerical models also showed a rapid wedge widening for the first 2–3 Myr, followed by a decrease in the wedge widening rate (Figure 6). As with the physical experiments, numerical simulations showed a wedge width that increased asymptotically toward a steady state width that varied inversely with K (Figure 6). The final wedge width difference between the high and low erosion cases in the numerical simulations is ~130 km.

4.2. Strain Analysis: Experimental Versus Numerical Models

[18] We used PIV to characterize the structural features of the experimental wedges and compare these results with the numerical simulations. In both modeling approaches and during the early stages of convergence, an initial "pop up"

structure develops that is limited by two conjugate shear bands or thrust faults (auxiliary material).[1] This structure consists of a forward verging shear band (fore-shear) and a backward verging shear band (back-shear), both of which grow simultaneously and take up the majority of the initial cumulative strain. Next, the wedge grows episodically [e.g., *Mulugeta and Koyi*, 1992] by developing new fore-shear bands that propagate deformation forward, and back-shear bands that adjust the wedge to its critical taper [*Dahlen*, 1984]. Figure 7 shows the cumulative shear strain for the physical experiments accommodated between 0 and 200 mm of convergence. In all cases, erosion has not yet been applied to the wedge, allowing an assessment of the reproducibility of the models under no-erosion conditions. These models develop approximately the same number of fore-shear bands, ranging from 5 to 6, and the cumulative shear strain during this first few interval of growth ranges between 550 and 750%. The width of the experimental orogen up to this interval of convergence is similar in all the models, ranging from 22.5 to 27.0 cm. (Figure 7).

[19] In the following interval, during which erosion was episodically applied in the physical experiments, the number of fore-shear bands on each model decreased as K increased. Models with K values of 2.3×10^{-7} m$^{0.2}$/yr, 2.3×10^{-6} m$^{0.2}$/yr, 1.2×10^{-5} m$^{0.2}$/yr, and 2.3×10^{-5} m$^{0.2}$/yr produce nine, eight, eight, and seven fore-shear bands, respectively. Figure 8 shows the effects of erosion on the kinematics of the sand wedge as differences in the distribution of cumulative shear strain accommodated between 300 and 500 mm of convergence. The cumulative shear strain accumulated at

---
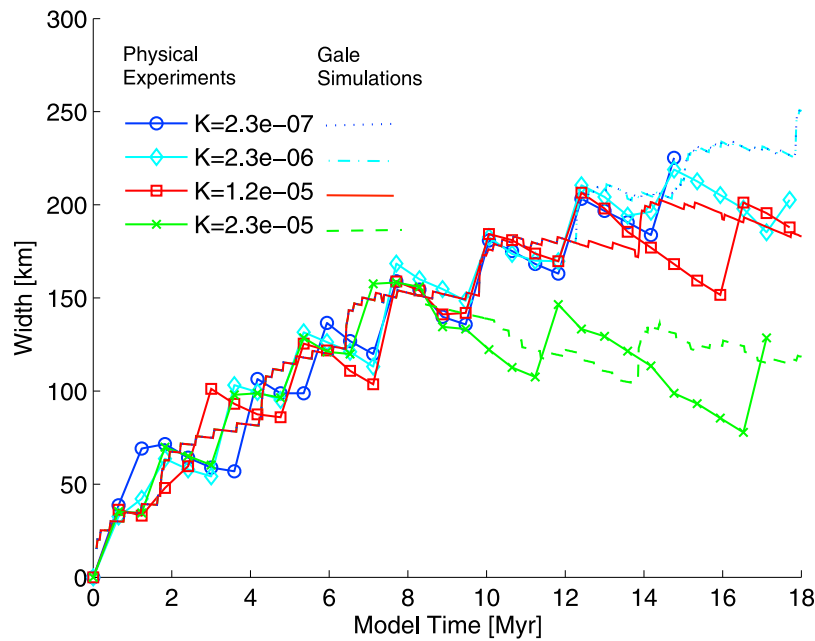[1]Auxiliary materials are available in the HTML. doi:10.1029/ 2010JB007472.

Figure 6. Temporal evolution of the scaled orogenic wedge width in the physical experiments (circles, diamonds, squares, and crosses correspond to the measurements of experimental geometries for K values of 2.3×10^{-7} $m^{0.2}$/yr, 2.3×10^{-6} $m^{0.2}$/yr, 1.2×10^{-5} $m^{0.2}$/yr, and 2.3×10^{-5} $m^{0.2}$/yr) and Gale numerical simulations (dotted, dash dotted, solid, and dashed lines correspond to the calculated theoretical simulations with K values of 2.3×10^{-7} $m^{0.2}$/yr, 2.3×10^{-6} $m^{0.2}$/yr, and 1.2×10^{-5} $m^{0.2}$/yr, and 2.3×10^{-5} $m^{0.2}$/yr, respectively).

a specific location in the sand wedge increases with K during this interval, while the number of shear bands formed during the experiment decreased. The highest strain value is observed in the models with relatively high erosion ($K = 2.3 \times 10^{-5}$ $m^{0.2}$/yr and 1.2×10^{-5} $m^{0.2}$/yr, in Figures 8c and 8d) with a peak cumulative shear strain of ~1050%, and the lowest strain value is observed in the relatively low erosion models ($K = 2.3 \times 10^{-7}$ $m^{0.2}$/yr and 2.3×10^{-6} $m^{0.2}$/yr, in Figures 8a and 8b) with a peak cumulative shear strain of ~750%.

[20] During model deformation and erosion in the physical experiments,, high erosion cases prevented initiation of new fore-shear bands and instead concentrated strain along those previously formed, which increased the duration and magnitude of slip along individual fore-shear bands. Conversely, low erosion cases favored formation of new fore-shear bands at the wedge's periphery, which distributed the total convergence across many structures that individually accommodated less total shear displacement.

[21] Similarly, in the Gale numerical simulations, the number of fore-shear bands observed in each model decreased as K increased (Figure 9). However, fewer fore-shear bands were generated in the numerical simulations relative to corresponding physical experiments. Models with K values of 2.3×10^{-7} $m^{0.2}$/yr, 2.3×10^{-6} $m^{0.2}$/yr, 1.2×10^{-5} $m^{0.2}$/yr, and 2.3×10^{-5} $m^{0.2}$/yr produce seven, seven, six, and five fore-shear bands, respectively. The cumulative strain accommodated by any one of the shear bands in the simulations also increased with K, producing the highest cumulative strain values in the models with relatively high erosion ($K = 2.3 \times 10^{-5}$ $m^{0.2}$/yr and 1.2×10^{-6} $m^{0.2}$/yr, in Figures 9c and 9d) with strain values close to 300%. The

lowest strain values are observed in the relatively low erosion models ($K = 2.3 \times 10^{-7}$ $m^{0.2}$/yr and 2.3×10^{-6} $m^{0.2}$/yr, in Figures 9a and 9b) with peak cumulative strain of 150–300% (Figure 9).

[22] Although variations between the numbers of shear bands exist between the numerical and physical experiments, the locus of deformation over time in both simulations is similar. For example, the high erosion cases show deformation largely accommodated along the second to last fore-shear band in the models with K values of 2.3×10^{-5} $m^{0.2}$/yr and 1.2×10^{-5} $m^{0.2}$/yr (Figures 9c, 9d, 8c, and 8d). The width of shear bands in the numerical simulations is greater than that of the physical experiments, and the dip and strain magnitude of the back-shear bands in the numerical simulations is stepper and greater, respectively, than those in the physical experiments. The greater width of shear-bands in the numerical simulation likely reflects the fact that the model grid spacing used was 5038 m due to computational constraints compared to 2775 m used in the PIV calculations. This broader zone of shear banding observed in the numerical model likely is responsible for the lower cumulative shear strain observed at a point within the shear bands (750% versus 300% for the experimental and numerical simulations, respectively). The overall dip of the fore-shear bands in both modeling approaches is similar (Figures 8 and 9). The thrust spacing in the numerical simulations is more regular than that observed in the physical experiment, where the frequency of thrusting increased in the early stages of deformation. In addition, the numerical simulations developed subdued, smooth topography, relative to the more rugged forms produced in the physical experiments (Figures 8 and 9).
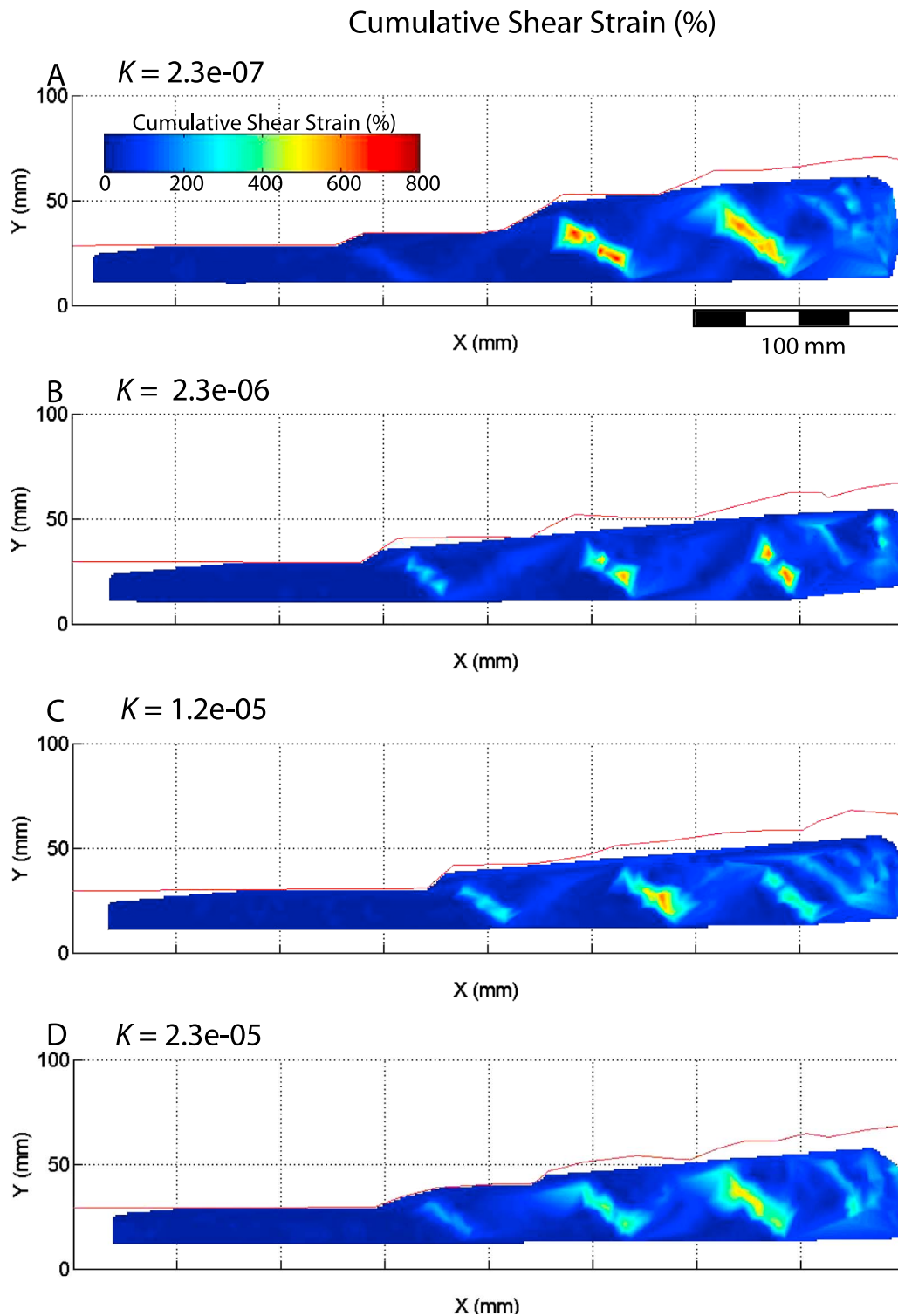
Figure 7. Cumulative shear strain calculated for a model displacement between 0 and 200 mm. The calculated strain values of the models ((a) $K = 2.3 \times 10^{-7}$ m$^{0.2}$/yr, (b) 2.3×10^{-6} m$^{0.2}$/yr, (c) $K = 1.2 \times 10^{-5}$ m$^{0.2}$/yr and (d) 2.3×10^{-5} m$^{0.2}$/yr) during this initial period of displacement during which the surface is uneroded range between 550 and 750% and show a similar number and position of fore-shear bands among the simulations.
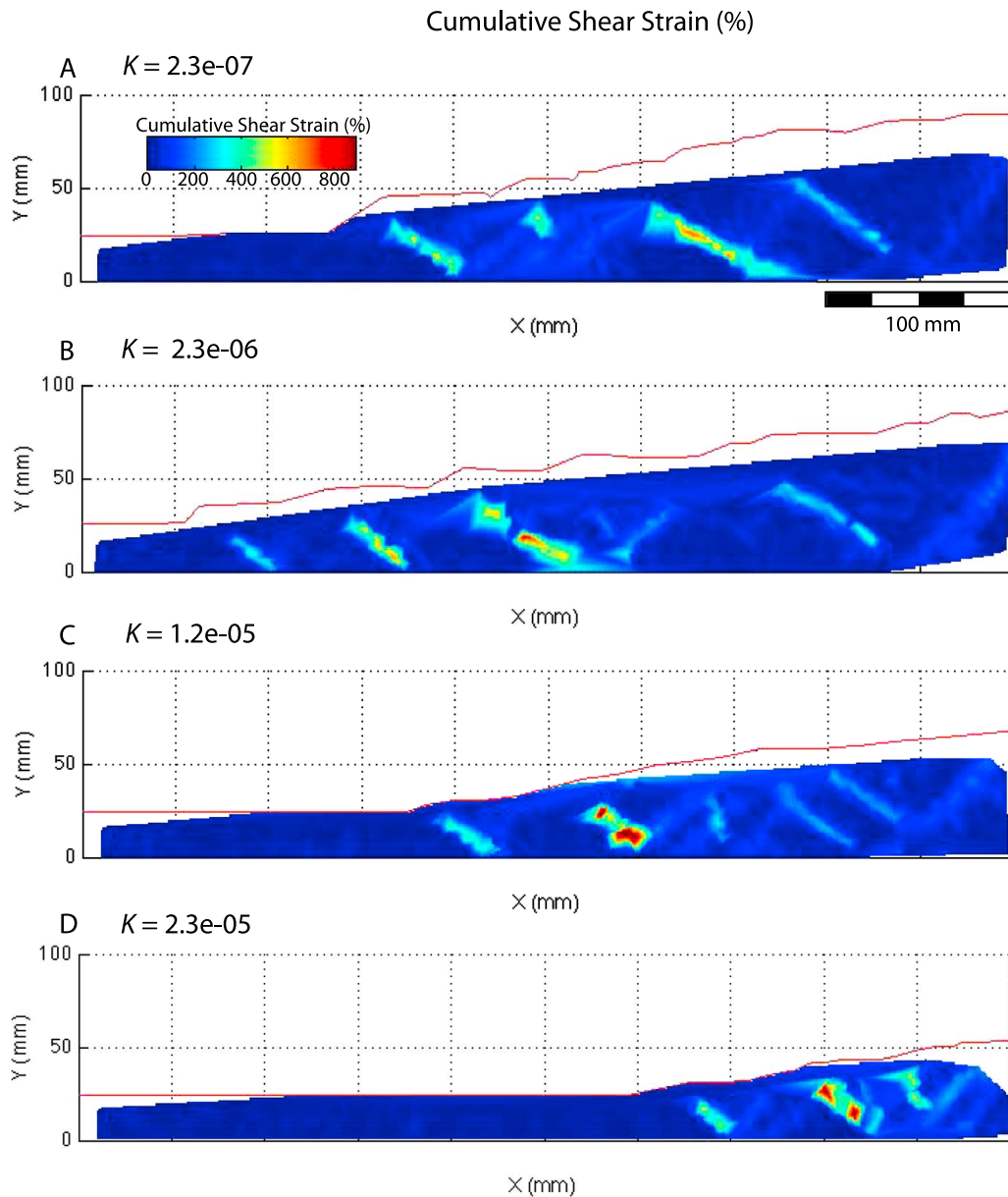
Figure 8. Cumulative shear strain calculated for interval of model displacement between 300 and 500 mm, during which the surface of the sand wedge was episodically eroded. The highest shear strain values were observed in the high K models (c) $K = 1.2 \times 10^{-5}$ m$^{0.2}$/yr and (d) 2.3×10^{-5} m$^{0.2}$/yr, showing a cumulative shear strain of ~1050%, while the lowest strain value is observed in the relatively low erosion models (a) $K = 2.3 \times 10^{-7}$ m$^{0.2}$/yr and (b) 2.3×10^{-6} m$^{0.2}$/yr that produced cumulative shear strain of ~750%.

[23] In the physical experiments, two or more fore-shear bands were never active at the same moment in time, although this has been reported to occur in low basal-friction experimental wedges [*Koyi et al.*, 2000]. However, in our physical experiments, multiple shear bands may be active over 1 Myr (scaled time) as shown in Figure 10. Beyond the initiation of three fore-thrusts (roughly ~5 Myr of model time) inactive fore-thrusts in all models are reactivated as out-of-sequence thrusts, as the wedge internally thickens to maintain a critical taper. Later, erosion increases the activity of these out-of-sequence thrusts (Figure 10), and

in some cases the reactivation occurs on shear bands located three to four structures in back of the front-most shear band. For example, models with moderate erosion ($K = 2.3 \times 10^{-6}$ m$^{0.2}$/yr) showed activity of shear bands eight and four (numbered from the backstop forward) between 14 and 16 Myr of model time while shear bands six and seven were inactive during that same period of time (Figure 10). Similarly, the numerical simulations showed reactivated out-of-sequence thrusts that are active after ~6 Myr of model time, and erosion also increases the activity of these thrusts (Figure 11). However, in these simulations, two or more
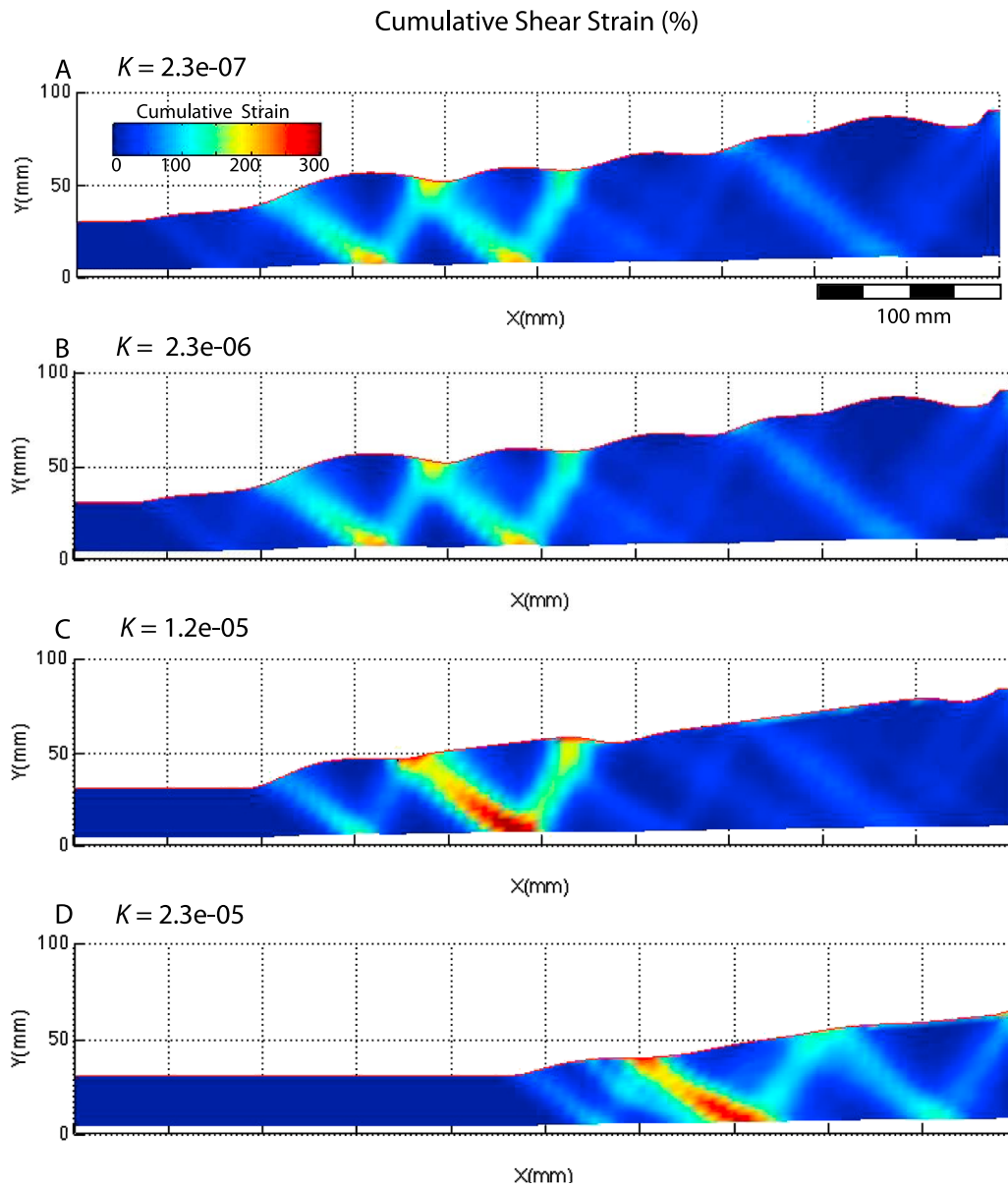
Figure 9. Cumulative shear strain calculated for interval of model displacement between 300 and 500 mm for the Gale numerical simulation, during which the surface of the sand wedge was episodically eroded. The highest shear strain values were observed in the high K models (c) $K = 1.2 \times 10^{-5}$ m$^{0.2}$/yr and (d) 2.3×10^{-5} m$^{0.2}$/yr, showing a shear strain of 300%, while the lowest strain value is observed in the relatively low erosion models (a) $K = 2.3 \times 10^{-7}$ m$^{0.2}$/yr and (b) 2.3×10^{-6} m$^{0.2}$/yr that produced cumulative strain of 150–200%.

fore-thrusts sometimes are active simultaneously, at least for the time increments used in the numerical simulations.

5. Discussion

[24] When studying erosion-tectonics interactions, several experimental studies have used different rules to model erosion in scaled mountain belts. Some physical experiments used rules that enforce spatially and temporally constant erosion rates, or others that maintain horizontal [e.g., *Cobbold et al.*, 1993; *Persson and Sokoutis*, 2002] or inclined erosion surfaces based on reference critical tapers [e.g., *McClay and Whitehouse*, 2004; *Konstantinovskaia and*

Malavieille, 2005]. Other sandbox simulations have successfully used an elevation-dependent erosion model [*Hoth et al.*, 2006, 2008], and others have used variable erosion rates applied parallel to the developed slope to produce steady state conditions [*Cruz et al.*, 2008]. While these rules may provide insight into erosion-tectonic coupling, more geomorphically realistic erosion rules, such as the one used in this work, can relate changes in erosional efficiency due to changing exposure of different rock types or climate to the distribution of deformation in a quantitative way. This opens up the potential of examining the manifestations of past climate changes in the kinematics of natural fold-and-thrust belts observed at the surface.
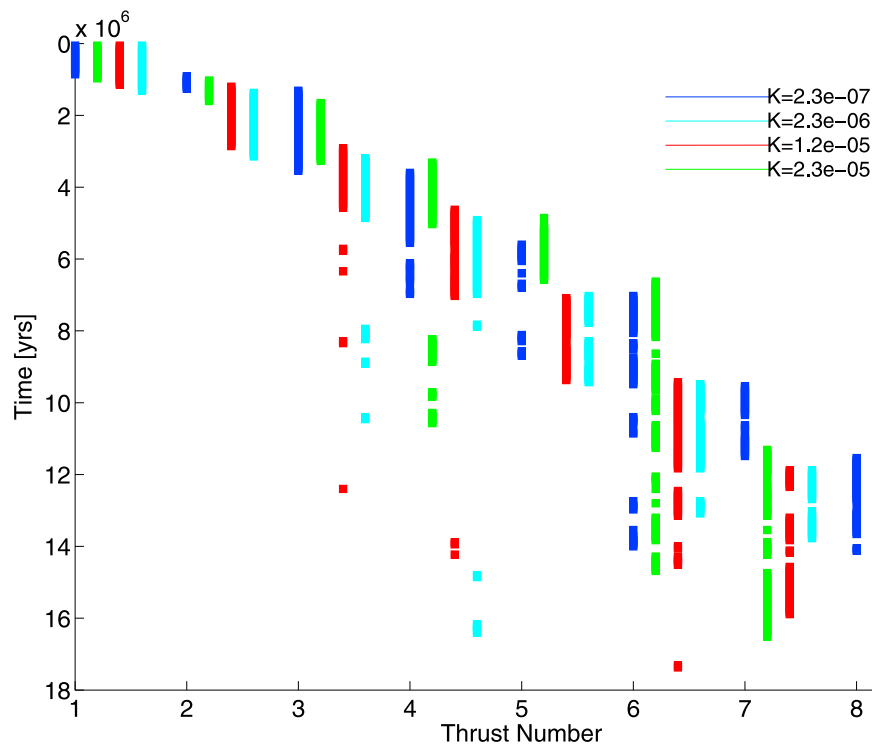
Figure 10. Time of active displacement along individual experimental fore-shear bands, showing reactivated (out-of-sequence) thrusts for the models with K values of 2.3×10^{-7} m$^{0.2}$/yr, 2.3×10^{-6} m$^{0.2}$/yr, 1.2×10^{-5} m$^{0.2}$/yr, and 2.3×10^{-5} m$^{0.2}$/yr. Thrusts are numbered in the order of their appearance, and so larger numbers reflect those thrusts that have been generated farther into the sand box than smaller numbers.

[25] The results obtained in this study indicate that mechanistic erosion rules [*Hilley et al.*, 2004; *Whipple and Meade*, 2004] can be applied to physical experiments of orogens to model mass removal. The orogen-wide erosion rule used in this study [*Hilley et al.*, 2004] is well suited for physical experiments because it assumes that the wedge grows regularly by maintaining a triangular cross section. The slope of the experimental sand wedge expected at the end of each time step can be easily achieved with a typical experimental setup. This experimental approach avoids more complicated mass removal procedures, which may include complex topographic shapes that are difficult to create [*Persson et al.*, 2004], and simplistic erosion rules that may not accurately represent erosional processes [e.g., *Cobbold et al.*, 1993; *Persson and Sokoutis*, 2002; *McClay and Whitehouse*, 2004; *Konstantinovskaia and Malavieille*, 2005; *Hoth et al.*, 2006; *Cruz et al.*, 2008; *Hoth et al.*, 2008]. The erosion rules used in this study produce realistic orogen widths and topographic slopes that are observed in nature e.g., fold-and-thrust-belt widths between 80 and 300 km (Aconcagua fold-and-thrust belt in Argentina [*Ramos et al.*, 2002], and the Serranía del Interior in Venezuela [*Hung*, 2005]). Our experiments produce topographic slopes that are also similar to those obtained in previous non-erosional physical experiments of frontally accreting wedges, e.g., topographic slopes between 6° and 15° [e.g., *Davis et al.*, 1983; *Koyi*, 1995; *Nieuwland et al.*, 2000; *Lohrmann et al.*, 2003], providing further validation to our experimental set-up.

[26] The observed growth of the eroded sand wedges in the experimental and numerical models is well predicted by theory [*Hilley et al.*, 2004], except for the high erosion case ($K = 2.3 \times 10^{-5}$ m$^{0.2}$/yr). We speculate that this behavior may be due to two experimental limitations. First, we assume that the wedge structure develops uniformly across the width of the experimental box, allowing measurements made at the sidewall to serve as proxies for the deformation sustained throughout the width of the entire apparatus. However, overhead photographs taken during the experiment indicate that the wedge width was greater in the center of the apparatus, as might be expected due to drag associated with sidewall friction. This effect would lead to an overestimation of basal fault angles and surface slopes when viewing only the sidewall profile. The incremental addition of this small error on the calculations might have affected the final width of that model. Second, previous experimental modeling of frontally accreting sand wedges has reported dissimilar wedge growth, producing progressive variations in the height/width ratio that is associated with a change in rheology of the sand due to compaction during deformation [*Koyi*, 1995]. This effect may have also contributed to the width difference of ~35 km after 18 Myr of model time between the physical experiment and the theory. However, the numerical simulations that included neither sand compaction nor sidewall friction showed a similar wedge width evolution to that observed in the physical experiments. Thus, it seems reasonable to conclude that neither effect can
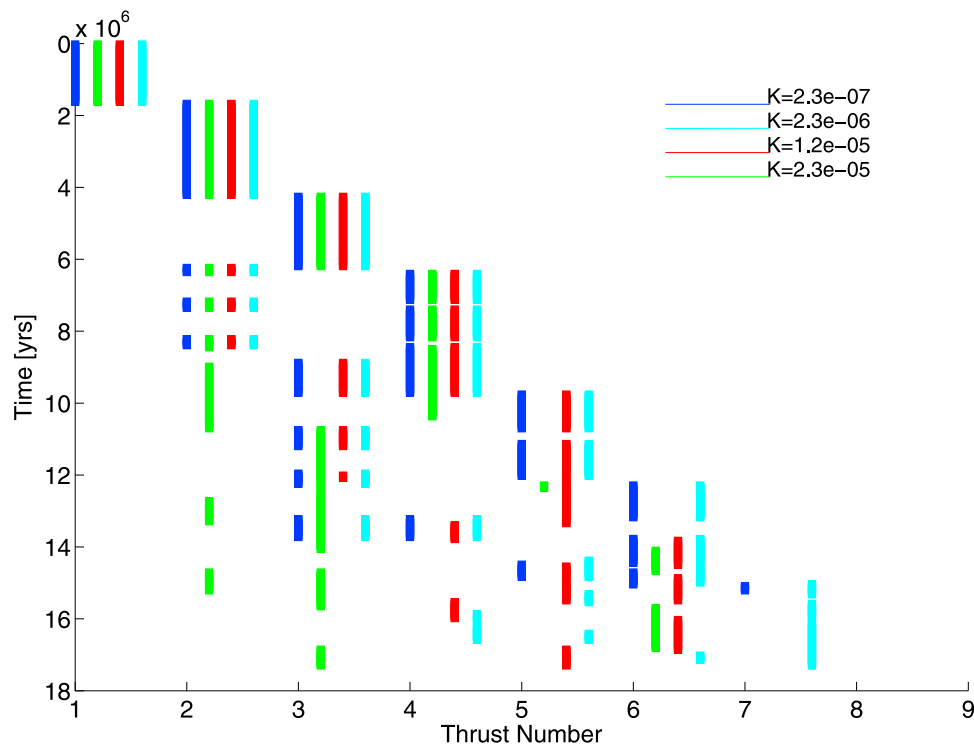
Figure 11. Time of active displacement along individual fore-shear bands modeled with Gale, showing reactivated (out-of-sequence) thrusts for the models with K values of 2.3×10^{-7} m$^{0.2}$/yr, 2.3×10^{-6} m$^{0.2}$/yr, 1.2×10^{-5} m$^{0.2}$/yr, and 2.3×10^{-5} m$^{0.2}$/yr. As in the Figure 10, thrusts are numbered in the order of their appearance. In contrast to the physical experiments, these numerical simulations show, after ~6 Myr of model time, two or more shear bands active simultaneously.

explain the misestimation of wedge width by the theoretical model.

[27] Another explanation or the mismatch between theoretical and physical/numerical experimental wedge geometries may result from the fact that the sand wedge does not continuously adjust to accretion and erosion as is assumed by theory, but instead does so by forming discrete, forward-propagating shear bands that episodically assimilate mass from the undeformed areas in front of the wedge into it. During our experiments, we observed that the formation of these forward-propagating shear bands was associated with an abrupt decrease in the load required to maintain constant displacement rate of the moving backstop (Figure 12). This implies that work must be performed to facilitate the initiation, propagation and linkage of the proto-fore-shear structures into a coherent shear zone. In this view, a shear band forms when the work required to elevate the topography exceeds that required to form a shear zone [e.g., *Masek and Duncan*, 1998; *Schott and Koyi*, 2001]. In the case of vigorous erosion, the slope of the topography may be maintained at sufficiently low values to prevent the formation of a new shear zone, forcing the wedge to deform in a supercritical state that is maintained over time. In this case, we might expect both physical and numerical experiments to under-predict wedge width relative to the theoretical model, which assumes that the energy associated with the shear-band formation is negligible.

[28] During the evolution of a fold-and-thrust belt, different lithologies with different resistances to erosion might be progressively exposed. *Stock and Montgomery* [1999] reported variations of several orders of magnitude in K values, depending on the types of rock being incised by rivers. We attempted to model this range in K values in our experiments. The large differences in the kinematics and geometries of our experiments suggests that the progressive exposure of different rock types in an evolving orogen may leave a profound imprint on these attributes of fold-and-thrust belts. Thus, we might expect that a fold-and-thrust belt that initially exposes low-resistance lithologies may grow in a supercritical manner within a restricted area, whereas the progressive exposure of deeper, more resistant lithologies might cause periods of rapid expansion of the topography of the fold-and-thrust belt that is accommodated by a larger number of structures that individually accommodate less slip.

[29] The use of this type of orogen-wide erosion rule has also allowed us to systematically quantify the effect of changing erosion intensity (K) on the kinematics of experimental and numerical fold-and-thrust belts modeled in a sandbox. We found a clear relationship between the erosion intensity and the number of fore-shear bands and strain magnitude. The number of fore-shear bands decreases while strain along each increases with erosion intensity. Previous experimental studies, although using different boundary conditions and less elaborated erosion rules, have also found
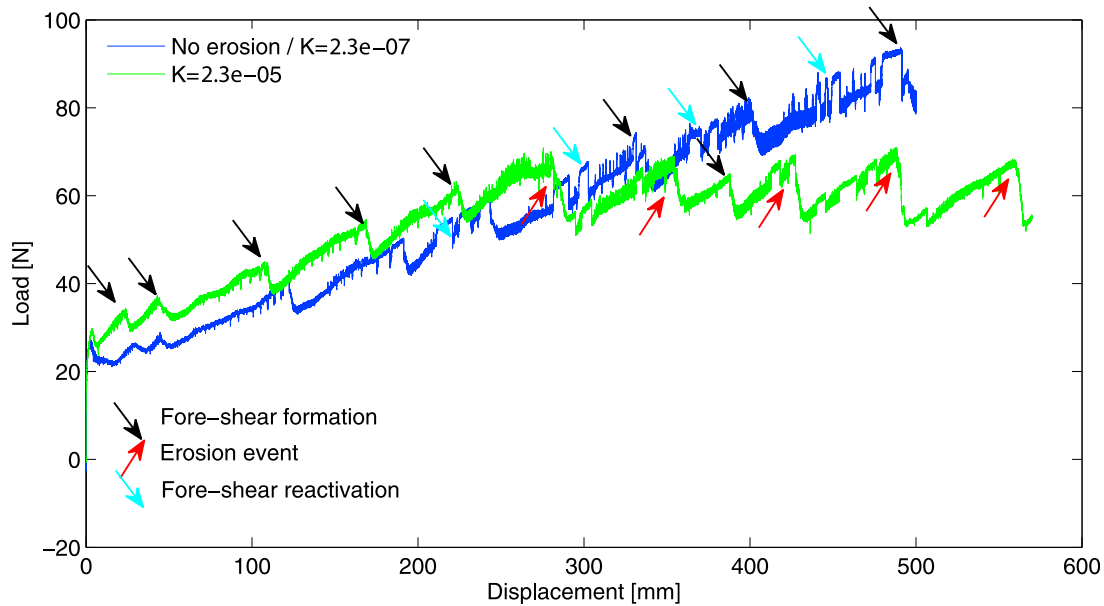
Figure 12. Load versus lateral displacement of the backstop for the models with K values of 2.3×10^{-7} m$^{0.2}$/yr and 2.3×10^{-5} m$^{0.2}$/yr. These experimental runs were performed under constant displacement rate boundary conditions. Note the abrupt decrease in the load required to maintain constant displacement rate of the moving backstop after the formation of a fore-shear band and after the removal of material (erosion).

that erosion prolongs the activity of faults [e.g., *Merle and Abidi*, 1995; *Cobbold et al.*, 1993; *Persson and Sokoutis*, 2002] and generates out-of-sequence thrusting [e.g., *Mugnier et al.*, 1997; *Leturmy et al.*, 2000; *Koyi et al.*, 2000; *Hoth et al.*, 2006]. Our systematic approach to quantifying the effect of changing erosion intensity on the geometry and kinematics of experimental fold-and-thrust belts may allow us to calibrate the strain history in fold-and-thrust belts to erosion intensities for a given set of wedge mechanical properties and geometries, and to use them to predict the geometric and kinematic history of a natural fold-and-thrust belt for different sets of erosional conditions.

[30] Results from our physical experiments and numerical simulations show that the deformation style and geometry of the fold-and-thrust belts are remarkably similar between the two. Shortening is mainly accommodated by in-sequence forward propagation of thrusting accompanied by out-of-sequence thrusting at several stages of deformation. This out-of-sequence thrusting accommodates wedge thickening in the hinterland over time and also occurs in the absence of erosion as the wedge propagates and adjust itself to reach a state of critical taper. However, increasing K clearly enhanced out-of-sequence thrusting to maintain the critical taper of the sand wedge. While wedge growth and topographic evolution are very similar between these modeling approaches, we observed some variability in the structural style, i.e., frequency of shear bands and enhanced back-shear strain magnitude, that may be related to node and particle resolution of the numerical code and/or issues with the numerical implementation of the selected rheology. This variability between our numerical and physical experiments is qualitatively similar but significantly less than that reported in previous analog-numerical benchmarking studies [*Buiter et al.*, 2006]. This is not unsurprising, as these

previous comparisons used a variety of physical and numerical modeling results whose boundary conditions and rheologies were not necessarily consistently maintained across all physical and numerical experiments.

6. Conclusions

[31] We successfully applied a mechanistic orogen-wide erosion rule to physical experiments of fold-and-thrust belts to model mass removal. This erosion law regards erosion rate as limited by the rate at which fluvial systems incise through bedrock. This approach proved well suited for physical experiments because it combined a realistic erosion law and a well-established wedge mechanical theory with simple experimental implementation. The utilization of such an erosion law allows the quantitative examination of differences in the kinematics of fold-and-thrust belts that might be expected to accompany changes in the exposure of different rock types or changes in climate.

[32] We systematically explored the effect of changing erosion intensity on the geometry and kinematics of the modeled fold-and-thrust belts and found that the experimental and numerical wedge growth is well predicted by theory. Additionally, we successfully quantified the two-dimensional kinematic response of these deforming wedges to changing erosional efficiency in the experimental fold-and-thrust belts, using PIV, and compared it with the kinematics calculated using the Gale model with identical rheologies and similar boundary conditions. We found that an inverse relationship exists between the erosion intensity and the number of fore-shear bands formed during the experiments. Likewise the shear strain magnitude accommodated by each shear band increased with erosional intensity. The large differences in kinematics observed for

different erosional conditions suggest that the kinematics of fold-and-thrust belts may reveal information about temporal changes in erosional efficiency in natural systems where these kinematics can be constrained.

References

Adam, J., J. Urai, B. Wieneke, O. Oncken, K. Pfeiffer, N. Kukowski, J. Lohrmann, S. Hoth, W. van der Zee, and J. Schmatz (2005), Shear localisation and strain distribution during tectonic faulting—New insights from granular-flow experiments and high-resolution optical image correlation techniques, *J. Struct. Geol.*, *27*(2), 283–301, doi:10.1016/j.jsg.2004.08.008.

Barr, T. D., and F. A. Dahlen (1989), Brittle frictional mountain building: 2. Thermal structure and heat budget, *J. Geophys. Res.*, *94*, 3923–3947, doi:10.1029/JB094iB04p03923.

Beaumont, C., P. Fullsack, and J. Hamilton (1992), Erosional control of active compressional orogens, in *Thrust Tectonics*, edited by K. R. McClay, pp. 1–18, Chapman and Hall, New York.

Buiter, S., A. Babeyko, S. Ellis, T. Gerya, B. Kaus, A. Kellner, G. Schreurs, and Y. Yamada (2006), The numerical sandbox: Comparison of model results for a shortening and an extension experiment, in *Analogue and Numerical Modelling of Crustal-Scale Processes*, edited by S. J. H. Buiter and G. Schreurs, *Geol. Soc. Spec. Publ.*, *253*, 29–64.

Byerlee, J. (1978), Friction of rocks: Rock friction and earthquake prediction, *Pure Appl. Geophys.*, *116*, 615–626, doi:10.1007/BF00876528.

Chapple, W. (1978), Mechanics of thin-skinned fold-and-thrust belts, *Geol. Soc. Am. Bull.*, *89*, 1189–1198, doi:10.1130/0016-7606(1978)89<1189:MOTFB>2.0.CO;2.

Cobbold, P. R., P. Davy, D. Gapais, E. A. Rossello, E. Sadybakasov, J. C. Thomas, J. J. Tondji Biyo, and M. de Urreiztieta (1993), Sedimentary basins and crustal thickening; Basin analysis and dynamics of sedimentary basin evolution, *Sediment. Geol.*, *86*, 77–89, doi:10.1016/0037-0738(93)90134-Q.

Cruz, L., C. Teyssier, L. Perg, A. Take, and A. Fayon (2008), Deformation, exhumation, and topography of experimental doubly vergent orogenic wedges subjected to asymmetric erosion, *J. Struct. Geol.*, *30*, 98–115, doi:10.1016/j.jsg.2007.10.003.

Dahlen, F. A. (1984), Noncohesive critical Coulomb wedges: An exact solution, *J. Geophys. Res.*, *89*, 10,125–10,133, doi:10.1029/JB089iB12p10125.

Dahlen, F. A., and T. D. Barr (1989), Brittle frictional mountain building: 1. Deformation and mechanical energy budget, *J. Geophys. Res.*, *94*, 3906–3922, doi:10.1029/JB094iB04p03906.

Dahlen, F. A., and J. Suppe (1988), Mechanics, growth, and erosion of mountain belts; Processes in continental lithospheric deformation, *Spec. Pap. Geol. Soc. Am.*, *218*, 161–178.

Dahlen, F. A., J. Suppe, and D. Davis (1984), Mechanics of fold-and-thrust belts and accretionary wedges: Cohesive Coulomb theory, *J. Geophys. Res.*, *89*, 10,087–10,101, doi:10.1029/JB089iB12p10087.

Davis, D., J. Suppe, and F. A. Dahlen (1983), Mechanics of fold-and-thrust belts and accretionary wedges, *J. Geophys. Res.*, *88*, 1153–1172, doi:10.1029/JB088iB02p01153.

DeCelles, P. G., and P. C. DeCelles (2001), Rates of shortening, propagation, underthrusting, and flexural wave migration in continental orogenic systems, *Geology*, *29*(2), 135–138, doi:10.1130/0091-7613(2001)029<0135:ROSPUA>2.0.CO;2.

England, P. C., and G. A. Houseman (1986), Finite strain calculations of continental deformation: 2. Comparison with the India-Asia collision zone, *J. Geophys. Res.*, *91*, 3664–3676, doi:10.1029/JB091iB03p03664.

Goodman, R. E. (1988), *Introduction to Rock Mechanics*, 2nd ed., 576 pp., John Wiley, New York.

Grujic, D., I. Coutand, B. Bookhagen, S. Bonnet, A. Blythe, and C. Duncan (2006), Climatic forcing of erosion, landscape and tectonics in the Bhutan Himalayas, *Geology*, *34*, 801–804, doi:10.1130/G22648.1.

Hilley, G. E., and M. R. Strecker (2004), Steady state erosion of critical Coulomb wedges with applications to Taiwan and the Himalaya, *J. Geophys. Res.*, *109*, B01411, doi:10.1029/2002JB002284.

Hilley, G. E., M. R. Strecker, and V. A. Ramos (2004), Growth and erosion of fold-and-thrust belts with an application to the Aconcagua fold-and-thrust belt, Argentina, *J. Geophys. Res.*, *109*, B01410, doi:10.1029/2002JB002282.

Hoth, S., J. Adam, N. Kukowski, and O. Oncken (2006), Influence of erosion on the kinematics of bivergent orogens: Results from scaled sandbox simulations, in *Tectonics, Climate, and Landscape Evolution*, *Spec. Pap. Geol. Soc. Am.*, *398*, 201–225.

Hoth, S., N. Kukowski, and O. Oncken (2008), Distant effects in bivergent orogenic belts; how retro-wedge erosion triggers resource formation in pro-foreland basins, *Earth Planet. Sci. Lett.*, *273*, 28–37, doi:10.1016/j.epsl.2008.05.033.

Howard, A. D., and G. Kerby (1983), Channel changes in badlands, *Geol. Soc. Am. Bull.*, *94*, 739–752, doi:10.1130/0016-7606(1983)94<739:CCIB>2.0.CO;2.

Hubbert, M. K. (1937), Theory of scale models as applied to the study of geologic structures, *Geol. Soc. Am. Bull.*, *48*, 1459–1520.

Hung, E. J. (2005), Thrust belt interpretation of the Serranía del Interior and Maturín subbasin, eastern Venezuela, in *Caribbean–South American plate interactions, Venezuela*, edited by H. G. Avé Lallemant and V. B. Sisson, *Spec. Pap. Geol. Soc. Am.*, *394*, 251–270, doi:10.1130/2005.2394(10).

Klinkmueller, M., M. Rosenau, D. Boutelier, H. Kemnitz, and G. Schreurs (2008), Properties benchmark of granular and viscous analogue materials, paper presented at International Geological Modelling Conference–GeoMod 2008, Florence, Italy.

Konstantinovskaia, E., and J. Malavieille (2005), Erosion and exhumation in accretionary orogens: Experimental and geological approaches, *Geochem. Geophys. Geosyst.*, *6*, Q02006, doi:10.1029/2004GC000794.

Koyi, H. (1995), Mode of internal deformation in sand wedges, *J. Struct. Geol.*, *17*, 293–300, doi:10.1016/0191-8141(94)00050-A.

Koyi, H. (1997), Analogue modeling: From a qualitative to a quantitative technique: A historical outline, *J. Pet. Geol.*, *20*, 223–238, doi:10.1111/j.1747-5457.1997.tb00774.x.

Koyi, H., K. Hessami, and A. Teixell (2000), Epicenter distribution and magnitude of earthquakes in fold–thrust belts: Insights from sandbox modeling, *Geophys. Res. Lett.*, *27*, 273–276, doi:10.1029/1999GL010833.

Leturmy, P., J. L. Mugnier, P. Vinour, P. Baby, B. Colletta, and E. Chabron (2000), Piggyback basin development above a thin-skinned thrust belt with two detachment levels as a function of interactions between tectonic and superficial mass transfer: The case of the Subandean Zone (Bolivia), *Tectonophysics*, *320*, 45–67, doi:10.1016/S0040-1951(00)00023-8.

Lohrmann, J., N. Kukowski, J. Adam, and O. Oncken (2003), The impact of analogue material properties on the geometry, kinematics, and dynamics of convergent sand wedges, *J. Struct. Geol.*, *25*, 1691–1711, doi:10.1016/S0191-8141(03)00005-1.

Masek, J. G., and C. C. Duncan (1998), Minimum-work mountain building, *J. Geophys. Res.*, *103*, 907–917, doi:10.1029/97JB03213.

McClay, K. R., and P. S. Whitehouse (2004), Analog modeling of doubly vergent thrust wedges, in *Thrust Tectonics and Hydrocarbon Systems*, edited by K. R. McClay, *AAPG Mem.*, *82*, 184–206.

Merle, O., and N. Abidi (1995), Approche expérimentale du fonctionnement des rampes émergentes, *Bull. Soc. Geol. Fr.*, *166*, 439–450.

Moresi, L. N., F. Dufour, and H. B. Muhlhaus (2003), A Lagrangian integration point finite element method for large deformation modeling of viscoelastic geomaterials, *J. Comput. Phys.*, *184*, 476–497, doi:10.1016/S0021-9991(02)00031-1.

Mugnier, J. L., P. Baby, B. Colletta, P. Vinour, P. Bale, and P. Leturmy (1997), Thrust geometry controlled by erosion and sedimentation: A view from analogue models, *Geology*, *25*, 427–430, doi:10.1130/0091-7613(1997)025<0427:TGCBEA>2.3.CO;2.

Mulugeta, G., and H. Koyi (1987), Three-dimensional geometry and kinematics of experimental piggyback thrusting, *Geology*, *15*, 1052–1056, doi:10.1130/0091-7613(1987)15<1052:TGAKOE>2.0.CO;2.

Mulugeta, G., and H. Koyi (1992), Episodic accretion and strain partitioning in a model sand wedge, *Tectonophysics*, *202*, 319–333, doi:10.1016/0040-1951(92)90117-O.

Nieuwland, D. A., J. H. Leutscher, and J. Gast (2000), Wedge equilibrium in fold-and-thrust belts: Prediction of out-of-sequence thrusting based on sandbox experiments and natural examples, *Geol. Mijnbouw*, *79*, 81–91.

Peltzer, G., and P. Tapponnier (1988), Formation and evolution of strike-slip faults, rifts, and basins during the India-Asia collision: An experimental approach, *J. Geophys. Res.*, *93*, 15,085–15,117, doi:10.1029/JB093iB12p15085.

Persson, K. S., and D. Sokoutis (2002), Analogue models of orogenic wedges controlled by erosion, *Tectonophysics*, *356*, 323–336, doi:10.1016/S0040-1951(02)00443-2.

Persson, K. S., D. Garcia-Castellanos, and D. Sokoutis (2004), River transport effects on compressional belts: First results from an integrated

analogue-numerical model, *J. Geophys. Res.*, *109*, B01409, doi:10.1029/2002JB002274.

Raffel, M., C. Willert, and J. Kompenhans (1998), *Particle Image Velocimetry—A Practical Guide*, 253 pp., Springer, Berlin.

Ramberg, H. (1967), Model experimentation of the effects of gravity on tectonics processes, *Geophys. J. R. Astron. Soc.*, *14*, 307–329.

Ramos, V. A., E. O. Cristallini, and D. J. Perez (2002), The Pampean flat-slab of the central Andes, *J. South Am. Earth Sci.*, *15*, 59–78, doi:10.1016/S0895-9811(02)00006-8.

Schellart, W. (2000), Shear test results for cohesion and friction coefficients for different granular materials: Scaling implications for their usage in analogue modeling, *Tectonophysics*, *324*, 1–16, doi:10.1016/S0040-1951(00)00111-6.

Schott, B., and H. Koyi (2001), Estimating basal friction in accretionary wedges from the geometry and spacing of frontal faults, *Earth Planet. Sci. Lett.*, *194*, 221–227, doi:10.1016/S0012-821X(01)00543-X.

Sonder, L. J., and P. C. England (1986), Vertical averages of rheology of the continental lithosphere: Relation to thin sheet parameters, *Earth Planet. Sci. Lett.*, *77*, 81–90, doi:10.1016/0012-821X(86)90134-2.

Stock, J. D., and D. R. Montgomery (1999), Geologic constraints on bedrock river incision using the stream power law, *J. Geophys. Res.*, *104*, 4983–4993, doi:10.1029/98JB02139.

Whipple, K. X., and B. J. Meade (2004), Controls on the strength of coupling among climate, erosion, and deformation in two-sided, frictional orogenic wedges at steady state, *J. Geophys. Res.*, *109*, F01011, doi:10.1029/2003JF000019.

Willett, S. D. (1999), Orogeny and orography: The effects of erosion on the structure of mountain belts, *J. Geophys. Res.*, *104*, 28,957–28,981, doi:10.1029/1999JB900248.

Willett, S. D., and M. T. Brandon (2002), On steady states in mountain belts, *Geology*, *30*, 175–178, doi:10.1130/0091-7613(2002)030<0175:OSSIMB>2.0.CO;2.

L. Cruz, G. Hilley, J. Malinski, and A. Wilson, Department of Geological and Environmental Sciences, Stanford University, 450 Serra Mall, Braun Hall, Bldg. 320, Stanford, CA 94305, USA. (leocruz@stanford.edu)

W. A. Take, Department of Civil Engineering, Queen's University, Kingston, ON K7L 3N6, Canada.